Journal of Nanobiotechnology

RESEARCH

Open Access

Glutathione responsive iNOS inhibiting polymeric prodrug for targeted Inhibition of angiogenesis

Houman Alimoradi[1,2*], Anita Fallah[1], Pascale Jespers[3,4], Nargis Bolaky[1], Françoise Gregoire[1], Helen Townley[5], Susanna Törnroth-Horsefield[6], Armin Shavandi[2], Laurence Dewachter[3,4] and Christine Delporte[1*]

Abstract

Background Inducible nitric oxide synthase (iNOS) is a key driver of aberrant angiogenesis in inflammatory conditions and cancer, making it an attractive therapeutic target. Nevertheless, its function can be affected by the complex immune responses and tumor microenvironment (TME). Hence, combinatorial treatment approaches that simultaneously target iNOS and immune-modulatory signaling are strongly recommended for cancer therapy. Moreover, the current iNOS inhibitors are limited by poor pharmacokinetics and a lack of selectivity.

Results To address these challenges, we developed a glutathione (GSH)-responsive iNOS-inhibiting polymeric prodrug (GRIP) decorated with betamethasone succinate (NP_{BeS}). These dual-function nanoparticles (NP_{BeS}) remain stable under physiological conditions but selectively release their payload in response to elevated GSH levels, a hallmark of the TME. Only upon activation by GSH, NP_{BeS} inhibits iNOS, as evidenced by suppressed lipopolysaccharide (LPS)-induced nitric oxide (NO) production in RAW 264.7 macrophages. NP_{BeS} also normalized vascular endothelial growth factor (VEGF)-mediated tube formation in HUVECs and 3T3-L1 fibroblast cell migration, and angiogenesis in the CAM assay, demonstrating its anti-angiogenic activity. Importantly, GRIP did not impair acetylcholine (ACh)-induced vasodilation in rat aorta, even at elevated concentrations, indicating preservation of eNOS function.

Conclusions This is the first report of a GSH-responsive polymeric prodrug system that leverages intracellular GSH for both controlled release of anionic therapeutic agents and in situ synthesis of an iNOS antagonist. Through these two complementary pathways, the system enables targeted, sustained anti-angiogenic effects and promotes vascular normalization. This dual-function platform holds strong potential for the treatment of cancer-associated angiogenesis.

Keywords Angiogenesis, Gluthatione-responsive prodrug, iNOS, Nitric oxide, Tumor microenvironment

*Correspondence:
Houman Alimoradi
houman.alimoradi@ulb.be
Christine Delporte
christine.delporte@ulb.be

Full list of author information is available at the end of the article

© The Author(s) 2026. **Open Access** This article is licensed under a Creative Commons Attribution-NonCommercial-NoDerivatives 4.0 International License, which permits any non-commercial use, sharing, distribution and reproduction in any medium or format, as long as you give appropriate credit to the original author(s) and the source, provide a link to the Creative Commons licence, and indicate if you modified the licensed material. You do not have permission under this licence to share adapted material derived from this article or parts of it. The images or other third party material in this article are included in the article's Creative Commons licence, unless indicated otherwise in a credit line to the material. If material is not included in the article's Creative Commons licence and your intended use is not permitted by statutory regulation or exceeds the permitted use, you will need to obtain permission directly from the copyright holder. To view a copy of this licence, visit http://creativecommons.org/licenses/by-nc-nd/4.0/.

Graphical Abstract

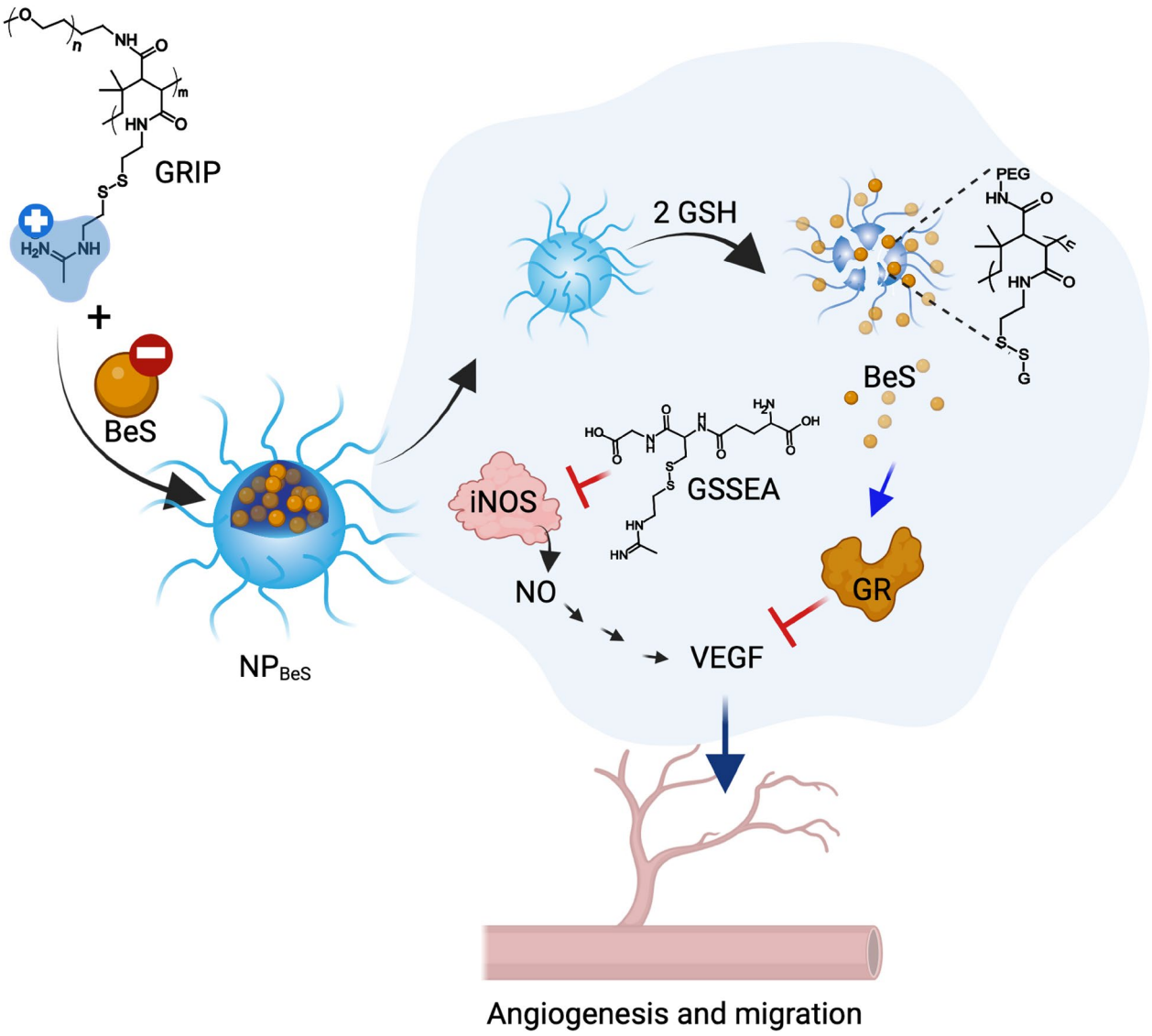

Background

Angiogenesis, the formation of new blood vessels from existing ones, plays a pivotal role in cancer progression, metastasis, and chronic inflammation [1]. To meet the increased demand for nutrients and facilitate the removal of metabolic waste and CO_2, tumor cells exploit physiological angiogenic mechanisms, driving neovascularization. Since tumors cannot grow beyond a few millimeters or metastasize without an adequate blood supply, targeting angiogenesis has been a cornerstone of cancer therapy for nearly five decades [1]. Despite significant efforts to develop anti-angiogenic therapies and their demonstrated efficacy in certain cancers, such as renal cell carcinoma, current treatments, even in combination with chemotherapy, generally yield only modest improvements in overall survival, extending life by weeks to a few months in patients with solid tumors [2].

Resistance to anti-angiogenic therapies arises from various adaptive or evasive mechanisms activated within the TME, largely driven by its hallmark features of hypoxia and persistent nutrient demand. To survive, tumors employ multiple strategies, including upregulation of antioxidant systems (e.g., elevated GSH levels), increased production of signaling molecules such as nitric oxide (NO), and secretion of pro-angiogenic growth factors like vascular endothelial growth factor (VEGF), fibroblast growth factors (FGFs), and transforming growth factor (TGF) to stimulate blood vessel formation. Furthermore, alternative modes of tumor vascularization, such as intussusception, vasculogenic mimicry, transdifferentiation of

cancer stem cells into endothelial-like cells, vasculogenic vessel growth, and vessel co-option, may emerge, many of which respond poorly to VEGF-targeted therapies [3].

Given the limited efficacy of conventional anti-angiogenic therapies, there has been a strategic shift toward vessel normalization strategies. These approaches aim to improve the structure and function of tumor vasculature by modulating key mechanisms within the TME [4]. Consequently, targeting additional signaling pathways that regulate tumor vasculature is essential to enhance clinical outcomes in cancer therapy.

NO is a critical signaling molecule involved in all forms of tumor vessel formation, including angiogenesis [5]. In humans, NO is synthesized from L-arginine by nitric oxide synthase (NOS), which exists in three isoforms: neuronal (nNOS), inducible (iNOS), and endothelial (eNOS) [6]. Although these isoforms share a common biochemical pathway for NO production, they differ in cellular distribution and activation mechanisms. eNOS is vital for cardiovascular homeostasis, whereas iNOS expression and activity are markedly elevated in pathological states such as inflammation and cancer [7]. Tumor vessel formation and NO signaling are intricately interconnected: elevated NO levels promote angiogenesis, while angiogenesis, in turn, enhances the expression and activity of eNOS and iNOS [8, 9]. As a result, NOS inhibition has been investigated for decades as a strategy to suppress tumor angiogenesis. However, the clinical utility of current NOS inhibitors is limited by poor tissue selectivity, and non-specific inhibition of NOS, especially of eNOS, can cause severe cardiovascular side effects, such as hypertension.

To address the unmet clinical need for more effective anti-angiogenic therapies, we developed GRIP, which selectively inhibits iNOS upon activation by GSH. Additionally, the cationic nature of GRIP enables it to serve as a delivery vehicle for hydrophobic drugs bearing anionic or acidic moieties, facilitating synergistic anticancer effects. We formulated nanoparticles (NPs) by complexing GRIP with betamethasone succinate (BeS), which exhibited remarkable GSH-responsiveness and potent anti-angiogenic activity both in vitro and in ovo.

Methods

Materials

Unless otherwise stated, all reagents utilized in this study were sourced from TCI-Belgium (Zwijndrecht, Belgium) or Merck (Sigma-Aldrich, St Louis, MI, USA). Solvents were procured from Thermo Fisher Scientific (Waltham, MA, USA) or Merck (Rahway, NJ, USA) and used as received, without additional purification. Nuclear magnetic resonance (NMR) spectra were recorded using a 400 MHz NMR instrument (JEOL, Tokyo, Japan) and analyzed using MestReNova software (v.15, CIREM licensed). Transmission electron microscopy (TEM) was carried out at CMMI center of ULB using Tecnai 10 100 kV instrument. Cell culture reagents were supplied by Thermo Fisher Scientific.

Synthesis of GRIP

To synthesize GRIP, we initially protected one of the amine groups of cystamine with di-tert-butyl dicarbonate (BOC anhydride) to make mono-BOC-protected cystamine. Cystamine dihydrochloride was solubilized in distilled water, and the pH was increased to 10 using 1 M NaOH. The solution was then extracted three times with ethyl acetate and evaporated to make cystamine. To a 20 mL solution of cystamine (75 mg/mL) in dichloromethane (DCM), 2.19 g of BOC anhydride (10 mmol, solubilized in 80 mL DCM) was added dropwise overnight. The resulting solution was worked up, and the organic layers were separated and evaporated to get 1.56 g of mono-BOC-protected cystamine as a white solid.

Next, 0.42 g (2.5 mmol) of poly (isobutylene-alt-maleic anhydride; PIMA; MW = 6 kDa) was reacted with 0.5 g of mono-BOC-protected cystamine in dichloromethane (DCM) for 4 h at room temperature. The reaction of mono-BOC-protected cystamine with the anhydride group makes an amide bond and a free acid group. The carboxylic groups of the resulting compound were activated with 0.38 g 1-ethyl-3-(3-dimethylaminopropyl) carbodiimide (EDC) and 0.35 g N-hydroxysuccinimide (NHS) and then reacted first with 0.4 g (0.067 mmol) methoxy polyethylene glycol amine (PEG-Amine, MW = 5 kDa), followed by an excess of mono-BOC-protected cystamine to form compound **2**.

To remove the BOC groups, 5 mL of trifluoroacetic acid (TFA) was added to 0.5 g of compound **2** (dissolved in 10 mL DCM) at room temperature and stirred for 4 h. The solvent was evaporated, and the resulting compound was dissolved in 15 mL of ethanol, followed by reaction with excess ethyl acetimidate in the presence of triethylamine (Et_3N). After 24 h, the solvent was evaporated, and the crude product was redissolved in a few drops of ethanol, followed by the addition of distilled water. The solution was dialyzed against distilled water using a 3.5 kDa molecular weight cut-off membrane for 72 h. The dialysate was then freeze-dried and stored at − 20 °C for further analysis or use.

Decorating GRIP with ionic molecules

NPs were prepared via ionic interactions between cationic GRIP and various anionic compounds (e.g., Eosin, Cy5.5, BeS, or carboxymethyl cellulose; CMC) as previously described [10]. Different weight ratios (w/w) of the cation and anion components were mixed in 1x phosphate-buffered saline (PBS) at pH 7.4 and vortexed vigorously for 30 min. The size and surface charge of the

resulting NPs were assessed using the Zetasizer Nano series (Malvern ZEN3600).

iNOS Inhibition assay

iNOS enzymatic activity was measured by quantifying the NO generated using a commercial iNOS activity kit containing 3.6 U/mL of iNOS in 50 mM HEPES buffer (4-(2-hydroxyethyl)-1-piperazineethanesulfonic acid), in the presence of NADPH (300 µM), magnesium acetate (1.0 mM), tetrahydrobiopterin (180 µM), and dithiothreitol (1.8 µM). The generated NO in the solution was quantified using the Griess assay [10]. To evaluate the effect of GSH on GRIP activity, compounds were pre-incubated with or without 5 mM GSH, followed by dialysis in a semipermeable sac (3.5 kDa cutoff) against distilled water for 24 h at room temperature. The resulting dialysate was freeze-dried and stored at -20 °C for further analysis.

Docking of GSSEA to human iNOS

Ethyl acetamidated GSH (GSSEA) and the reaction product formed between GRIP and cysteine (CySSEA) was docked to the crystal structure of the catalytic domain of human iNOS (PDB code 4NOS, chain A) using the Attracting Cavities option in SwissDock 2024 [11, 12] with the following settings: box size 25, 20, 20, sampling exhaustivity medium, cavity prioritization buried, and number of RIC 1. For GSSEA, 49 clusters of docking solutions were obtained, which were evaluated based on the Attracting Cavities (AC) score and SwissParam score. The best member of the top cluster (cluster 0) scored better on both these scores compared to all other clusters (Table S1). The figure showing the docking results was made using PyMOL (version 2.3.1, Schrödinger LLC).

Eosin release study from GRIP-based NPs

A nanosized polyionic complex was formed by combining GRIP with eosin, a traceable acidic molecule, at a weight ratio of 2:1 (GRIP: eosin) to achieve a neutral surface charge. The formulation was dialyzed against distilled water for 48 h and then lyophilized to get a reddish powder. A 1 mg/mL solution of GRIP-Eosin was used to track the release of negative compound (tracible compound) from the decorated GRIP using the dialysis technique. Hence, 2 mL of GRIP-Eosin solution (1 mg/mL) was prepared in PBS at different pH values (6.0, 7.4, and 8.0) or in the presence of 10mM of GSH and kept inside small sacs made of dialysis membrane with a molecular weight cut-off of 3.5 KDa. Then, these sacs were submerged in 40 mL of PBS, and the release of eosin was tracked by measuring the absorbance at 520 nm using a spectrophotometer (Spark® multimode microplate reader).

Cell culture

Three different cell types were used in this study: murine fibroblasts (3T3-L1, ATCC, Manassas, VA, USA), murine macrophages (RAW264.7, ATCC), and human umbilical vein endothelial cells (HUVECs, ATCC, Passage 6–8). 3T3-L1 and RAW264.7 cells were cultured in Dulbecco's Modified Eagle Medium (DMEM) supplemented with 10% fetal bovine serum (FBS), 100 units/mL penicillin and 100 µg/mL streptomycin. HUVECs were grown in endothelial growth medium (CRL-1730™, ATCC) following the manufacturer's guidelines, containing human epidermal growth factor (hEGF), VEGF, human fibroblast growth factor-B (hFGF-B), R3-insulin-like growth factor-1 (R3-IGF-1), with additional supplementation of 10% FBS, 100 units/mL penicillin and 100 µg/mL streptomycin. All cells were maintained as monolayers in a humidified incubator set to 37 °C, with a 5% CO_2 atmosphere.

Cell viability assay

To assess cell viability, RAW264.7 cells were plated in 96-well plates at a density of 5,000 cells per well and allowed to proliferate for 24 h. Cells were then treated with varying concentrations of the tested compounds for 48 h. After treatment, the culture medium was discarded and replaced with 100 µL of a 0.4 mg/mL MTT solution (3-(4,5-dimethylthiazol-2-yl)-2,5-diphenyltetrazolium bromide) in fresh medium. Following a 3 h incubation, the medium was removed, and the resulting formazan crystals were dissolved in 100 µL of DMSO. Absorbance was measured at 540 nm using a plate reader (Victor X2, PerkinElmer, Waltham, MA, USA) to determine cell viability.

In vitro scratch cell migration assay

A scratch assay was used to assess the effects of NPs on VEGF-induced migration. NIH 3T3-L1 cells (1×10^5) were seeded in 24-well plates and allowed to grow for 12 h. The medium was then replaced with fresh medium containing 1% FBS, and cells were incubated for an additional 12 h. Once confluence was reached, cells were scratched with a sterile 200 µL pipette tip to generate a uniform gap. Cellular debris was removed by gentle rinsing with PBS. Cells were subsequently treated with VEGF alone (50 ng/mL) or in combination with GSSEA (equal amount to base of NPs), BeS (10 µM), or NPBeS (10 µM) for a further 12 h in fresh medium containing 0.5% FBS. Images of the scratched area were acquired at 0 and 12 h using an LSM900 microscope with Airyscan (Carl Zeiss, Oberkochen, Germany) using a 10× objective. Scratch width was quantified using ImageJ software, and migration was expressed as the percentage of scratch closure. Representative cells were stained with phalloidine 0.4 and DAPI (1 µM) and imaged using the microsope.

Fluorescent detection of NO generation

RAW264.7 cells were seeded at a density of 10,000 cells/well in 96-well microscopy plates and incubated for 24 h. Cells were then treated with various concentrations of the tested compounds for 4–24 h, followed by staining with 4 μM 4,5-diaminofluorescein-2 diacetate (DAF-2Da), a fluorescent probe for NO, for 45 min at 37˚C. Excess DAF-2Da was removed by washing the cells twice with fresh medium. Imaging was performed under controlled CO_2 and temperature conditions using an LSM900 microscope with Airyscan (Carl Zeiss) using a 20x objective.

Immunofluorescence of iNOS and vimentin

10,000 cells/well were seeded into 8-well chamber slides and incubated for 24 h, followed by treatment with VEGF (50 ng/ml) alone or in combination with GSSEA, BeS (10μM), or NP_{BeS} (10μM) for an additional 24 h. Cells were then washed with ice-cold PBS, fixed with 4% formaldehyde in PBS on ice for 15 min, and permeabilized with 0.1% Triton X-100 in PBS at room temperature for 5 min. After three PBS washes, samples were blocked with 5% goat serum in PBS for 1 h. Cells were incubated with rabbit primary antibodies against iNOS (1:65, PA3-030 A, ThermoFisher) and vimentin (1:100; #5741, Cell Signaling Technology, Danvers, MA, USA) diluted in 5% blocking buffer for 12 h at 4 °C. Afterward, samples were incubated with a fluorescent anti-rabbit secondary antibody (1:1000, #7074, Cell Signaling Technology) for 1 h in a dark, humidified chamber at room temperature, followed by nuclear staining with DAPI (1 μg/mL) for 5 min. After drying, slides were mounted with ProLong™ Gold (Thermo Fisher Scientific) and visualized using confocal microscopy (LSM900 with Airyscan; Carl Zeiss). Fluorescence intensity was analysed using ImageJ and normalized to cell number based on nuclear counts.

iNOS western blotting

To assess iNOS expression, cells were collected 24 h after treatment with LPS (500 ng/ml) alone or in combination with equal amount of GSSEA, BeS (10 μM), or NPBeS (10 μM) and lysed in a 50 mM Tris-HCl buffer containing 150 mM NaCl, 0.05% SDS, 1% Triton X-100, and a protease inhibitor cocktail (Thermo Fisher Scientific). Total protein concentrations were quantified using the BCA Protein Assay Kit (Thermo Fisher Scientific). For immunoblotting, 25 μg of protein per sample was combined with loading buffer containing 1% β-mercaptoethanol, denatured at 100 °C for 10 min, and separated on a 12% SDS-PAGE gel. Proteins were transferred onto PVDF membranes (Invitrogen, Carlsbad, CA, USA), which were then blocked in PBS-T (0.1% Tween 20 in PBS) with 5% non-fat dry milk for 1 h at room temperature. Membranes were incubated overnight at 4 °C with a rabbit anti-iNOS primary antibody (1:450, #PA3-030 A, Thermo Fisher Scientific), followed by a 1 h incubation with HRP-conjugated anti-rabbit secondary antibody (1:3000, #7074, Cell Signaling Technology) diluted in PBS-T with 5% milk at room temperature. After three washes with PBS-T, signal was detected using enhanced chemiluminescence (ECL) reagents (5 min, RT), and bands were visualized with the Amersham Imager 600 system (GE Healthcare Life Sciences, Malborough, MA, USA). Semi-quantitative analysis of iNOS expression was performed using the ratio of iNOS bands to the β-actin through gel analysis by Fiji (ImageJ).

HUVEC tube formation assay

Matrigel solution was thawed on ice and gently dispensed into a 96-well plate, followed by a 1 h incubation at 37 °C to allow hydrogel formation. Then, 10,000 HUVECs suspended in medium containing 5% FBS were added to each well and treated with VEGF (50 ng/ml) alone or in combination with GSSEA, BeS (10μM), or NP_{BeS} (10μM). After 24 h of incubation at 37 °C, tubular structures were imaged under a microscope and quantitatively analyzed using the Angiogenesis Analyzer plugin in Fiji (ImageJ).

Chick chorioallantoic membrane (CAM) assay

Fertilized Race Leghorn blanc chicken eggs were obtained from Kwekerij van het Hallerbos (Halle, Belgium). Eggs were gently washed with 37 °C water for a few minutes to remove dirt and debris, dried with clean tissues, and incubated in a MultiQuip Incubator at 37 °C with 60% humidity. After 60 h incubation, the eggs were disinfected with 70% ethanol, the shells carefully cracked, and the embryos transferred to plastic weighing boats covered with disinfected parafilm. The embryos were returned to the incubator at 37 °C for 24 h, during which dead and damaged embryos were excluded. To assess the effects of the tested compounds on angiogenesis, 6 mm filter discs (Whatman filter paper no. 5) soaked with VEGF (100 ng/embryo), either alone or in combination with other compounds, were applied topically onto the CAM. After 24 h, CAMs were imaged using a Nikon SMZ 745 camera (Tokyo, Japan), and angiogenesis was quantified by measuring the number of branches, number of junctions, and total length. The embryos tested during the treatment procedure were at Hamburger–Hamilton (HH) stages 20–22.

Vasoreactivity assay

The study (protocol acceptation number 921N) was approved by the Institutional Animal Care and Use Committee at the Faculty of Medicine, Université Libre de Bruxelles (Brussels, Belgium) and conducted in accordance with the guidelines of *the Guide for the Care and Use of Laboratory Animals* (NIH Publication No. 85 – 23, revised 1996). Male Wistar rats (weighing 421 ±

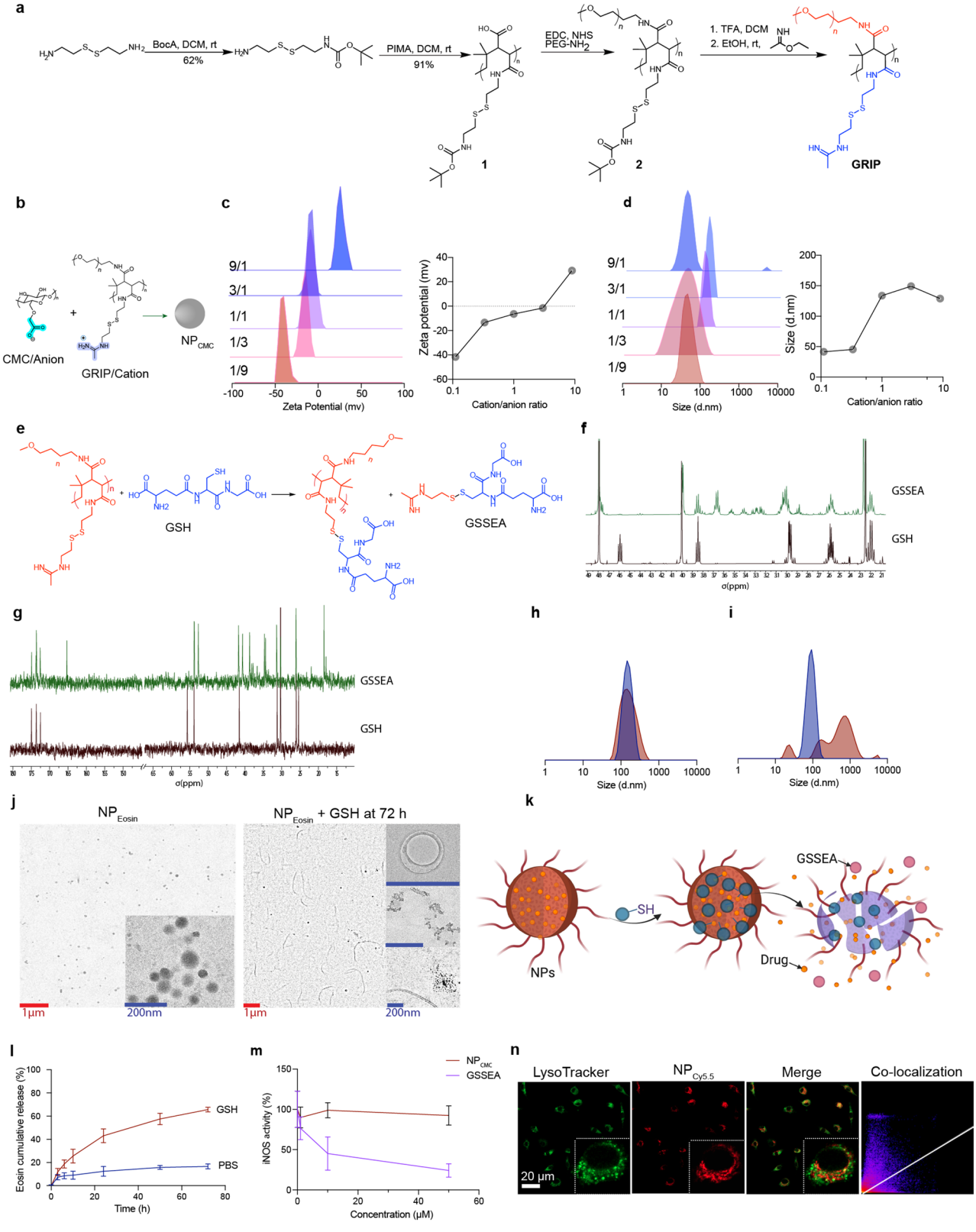

Fig. 1 (See legend on next page.)

(See figure on previous page.)

Fig. 1 GRIP is a GSH-responsive polymer that forms nanosized polyionic nanoparticles (NPs), enabling controlled drug release, selective iNOS inhibition, and efficient intracellular delivery. **(a)** Synthesis of GRIP. **(b)** GRIP forms NPs upon interaction with ionic polymers or molecules. For example, the interaction between GRIP (cation) and carboxymethyl cellulose (CMC, anion) leads to the formation of NP_{CMC}. **c & d.** Surface charge and size distribution of NPs synthesized at varying GRIP to CMC ratios. The average size of NPs increases with higher cation/anion ratios. **e.** Mechanism of GRIP activation by GSH leading to ethyl acetamidated GSH (GSSEA). **f & g.** Characterization of GSSEA synthesis using ^{1}HNMR and ^{13}CNMR, confirming the reaction between GSH and GRIP after 6 h of incubation at 37 °C. **h.** NP_{Eosin} exhibits an average size of approximately 170 nm and remains stable in PBS for at least 72 h. **i.** Exposure to 5 mM GSH results in increased polydispersity (Figure S2) and size of the NP_{Eosin}. **j.** TEM images of NP_{Eosin} and NP_{Eosin} when exposed to 5mM GSH for 72 h. **k.** Schematic representation illustrating how NP_{Eosin}, composed of GRIP and the acidic/anionic payload, functions as a GSH-responsive drug carrier. Created by BioRender.com. **l.** The release of Eosin Y from NP_{Eosin} in the presence or absense of 5mM GSH. **m.** Antagonistic activity of iNOS by GRIP (NP_{CMC}) and its GSH-activated form, GSSEA. GRIP exhibits no inhibition up to 50 µM, whereas GSSEA significantly inhibits iNOS at 10 µM ($p = 0.047$) and more strongly at 50 µM ($p = 0.008$). **n.** Cellular uptake of GRIP NPs labeled with Cy5.5 ($NP_{cy5.5}$), evaluated using confocal microscopy in the presence or absence of LysoTracker. The colocalization analysis showed the lack of overlap between the Cy5.5 (red) and LysoTracker (green) signals, suggesting endosomal escape or cytosolic delivery. Data are expressed as mean ±SD ($n = 3$) Created with BioRender.com

11 g) were obtained from Janvier (Le Genest Saint-Isle, France).

The effects of the treatments on vascular tone were evaluated using rat thoracic aortic rings, as previously described [13]. In brief, rats were euthanized by exsanguination (abdominal aorta transection) under deep inhaled anesthesia with 5% isoflurane. The thoracic aorta was dissected, cleared of blood, and cut into 2.7–3.8 mm-length transverse rings with intact endothelium. Rings were placed in Krebs-Henseleit solution (118 mmol/L NaCl, 4.7 mmol/L KCl, 1.2 mmol/L $MgSO_4$, 1.2 mmol/L KH_2PO_4, 2.5 mmol/L $CaCl_2$, 25 mmol/L $NaHCO_3$, 5.1 mmol/L glucose), bubbled with 95% O_2 and 5% CO_2 and maintained at 37 °C under 1 g of baseline resting tension. After a 20-minute equilibration period, contractile responses were first tested with 80 mmol/L KCl. Following washout, contraction was induced using 1 µmol/L phenylephrine hydrochloride (PE). Endothelium-dependent vasorelaxation was then evaluated with acetylcholine (ACh; 10^{-7} mol/L; Sigma-Aldrich, StLouis, Mo, USA) in PE-precontracted rings. Vessels that did not respond more than 65% of the contraction induced by phenylephrine were excluded from the study. After another washout and return to baseline tone, this protocol was repeated with PE-induced contraction and acetylcholine-mediated vasorelaxation, and then the effects of the treatments on the vascular tension were recorded using an isometric force transducer (connected to a data acquisition system; EMKA Technologies, Paris, France).

Data analysis

Data were expressed as means ± standard deviations (SD). Statistical analyses were carried out using GraphPad Prism v9 (Boston, MA, USA). Depending on data distribution, group differences were assessed using either one-way ANOVA or the Kruskal–Wallis test. Differences were considered significant if $p < 0.05$.

Results and discussion

The results from the synthesis and evaluation of GSH-responsiveness, as well as the in vitro, in ovo, and ex vivo studies on rat aorta, are presented below. The following subsections provide a detailed analysis of these key findings, beginning with the synthesis of GRIP.

Synthesis of GRIP

As depicted in Fig. 1a, the synthesis of GRIP involves three main steps: (i) formation of a mono-BOC-protected intermediate; (ii) reaction of this intermediate and PEG-Amine with PIMA to yield compound 2; and (iii) deprotection of the BOC groups, followed by conversion of the free amine in cystamine to an acetimidate. The ^{1}HNMR spectrum of PIMA, the backbone of GRIP, displays two –CH– proton signals at 3.27 and 3.10 ppm (Figure S1, Supporting Information). In GRIP, these signals shift upfield and appear at (a) 2.71 and (b) 2.32 ppm. GRIP also exhibits a distinct peak at 3.73 ppm, corresponding to the alkyl groups of the conjugated PEG-Amine. Additional new peaks observed at 3.66, 3.24, and 3.01 ppm are attributed to the $–CH_2–$ protons of cystamine. The methyl group ($–CH_3$) of the acetimidate appears at 2.28 ppm.

Decorating GRIP with anionic molecules

Polyionic complex NPs, often referred to as polyelectrolyte NPs, are a class of nanomaterials formed by the interaction between positively and negatively charged polymers. These electrostatic forces drive their self-assembly of the polymers into stable structures like micelles, vesicles, or core-shell configurations. Thanks to their ability to encapsulate charged therapeutic compounds, such as anticancer agents, antimicrobial substances, and imaging dyes, these NPs have found broad use in biomedical research [14–16]. The remarkable versatility of these NPs stems from the ease with which their properties can be customized. By varying factors such as polymer chain length, charge ratio, or incorporating specific chemical groups like metal-binding moieties, it is possible to precisely control the size, stability, and responsiveness of these NPs to biological signals [14–16].

When dissolved in water, GRIP contains a cationic charge due to its acetimidate groups, enabling it to be decorated with anionic molecules and/or polymers. For instance, upon mixing GRIP with CMC, polyionic complexes with nano-range sizes (NP_{CMC}, Fig. 1b) were

formed, as shown by DLS. The surface charge (Fig. 1c) and average size (Fig. 1d) of the resulting NPs depend on the ratios of cation (GRIP) to anion (CMC). By increasing the cation ratio from 1/9 to 9/1, the zeta potential shifted from − 41 mV to + 29 mV. At the 3/1 ratio, the particles exhibited a neutral surface charge and showed the largest diameter, with an average size of 149 nm. In addition, polydispersity index (PDI) of the particles at this ratio showed the lowest among all other formulations and this indicates the formation of more uniform NPs (Figure S2). NPs with neutral zeta potential, particularly those with PEG on their surface, offer higher stability under physiological conditions by minimizing interactions with proteins and immune recognition [17, 18]. Hence, neutral-surface-charge NPs were selected for subsequent biological testing.

GSH-responsive drug release and iNOS Inhibition

The concentration of GSH is elevated in some tumor types, such as breast, brain, ovarian, and lung cancer, compared to normal tissues [19]. For example, GSH levels per gram of wet tissue weight were found to be approximately twofold higher in breast tumors and up to fourfold higher in lymph node metastases than in corresponding normal tissue [20]. Further, intracellular GSH levels (1–10 mM) are approximately 1000-fold greater than the extracellular compartment (2–20 μM) [21]. Hence, GSH-responsive drug delivery systems take advantage of the elevated intracellular GSH levels characteristic of cancer cells to achieve targeted and controlled release of therapeutics [21, 22]. These systems commonly incorporate disulfide bonds that are specifically cleaved by GSH, leading to NPs breakdown or release of their payload within the TME.

To assess the GSH-responsiveness of GRIP, we initially tested whether GRIP could react with GSH to form a biologically active molecule capable of inhibiting iNOS. A 10 mg/mL solution of GRIP in PBS was incubated with 5 mM GSH at 37 °C for 6 h (Fig. 1e). After incubation, the reaction mixture was dialyzed, and the dialysate was subsequently concentrated and precipitated by ethanol addition. The resulting product was analyzed by NMR spectroscopy, confirming the formation of ethylacetimidated GSH (GSSEA). This was indicated by a shift in the α-proton of cysteine from 4.6 ppm in GSH to 4.8 ppm in GSSEA, along with the appearance of two additional proton signals at 3.0 ppm and two protons at 3.6 ppm (Fig. 1f and Figure S3). FT-IR analysis confirms the conversion of the thiol of GSH to a disulfide bond, as evidenced by the disappearance of the S-H stretching vibration at 2528 cm^{-1} (Figure S4). Furthermore, ^{13}C NMR analysis confirms the presence of disulfide ethyl acetimidamide transfer (Fig. 1g). In a more biologically relevant condition, 10 mg/mL solution of PIP was exposed to 5 mM GSH for 24 h and then the formation of GSSEA was assessed by high-resolution mass spectroscopy (HRMS) as 423.1320 (+ H+; Figure S5).

To further evaluate GSH-responsive drug release from the NPs formulated from GRIP, we electrostatically conjugated GRIP with an acidic dye (EosinY) to form NP_{Eosin} and assessed the dye release under different conditions. NP_{Eosin} showed an average size of 170± 39 nm in PBS, which remained stable over 72 h (Fig. 1h). The PDI of the NPs in PBS remained unchanged over this period, even under high salt stress (0.2 M NaCl; Figure S6), indicating good colloidal stability. In contrast, in the presence of 5 mM GSH under the same conditions, a significant increase in both particle size and PDI was observed (Fig. 1i and Figure S6).

TEM imaging of NP_{Eosin} revealed spherical particles with an average diameter of 81 nm, which is substantially smaller than the size measured by DLS. This discrepancy can be attributed to the hydration and solvation layers surrounding the particles in solution, which contribute to the hydrodynamic diameter measured by DLS.

Upon exposure to 5 mM GSH for 72 h, TEM images showed a marked decrease in electron density, and substantially fewer particles were detected at the same concentration (1 mg mL^{-1}). Moreover, the morphology of the detectable structures differed significantly from that of intact NP_{Eosin} particles. Indeed, elongated strand-like structures, very small particles, and occasional residual NPs were observed. These changes are likely due to alterations in the ionic structure of GRIP (upon reaction with GSH), leading to the disassembly of polyionic complexes and reduced electron contrast relative to the background (Fig. 1j). This activation process is schematically illustrated in Fig. 1k, where interaction of the GRIP-containing polyionic complexes with GSH results in GSSEA formation, accompanied by disruption of the NP structure.

The release of eosin from NP_{Eosin} was assessed using a dialysis technique in the presence or absence of 5 mM GSH. NP_{Eosin} demonstrated high stability in PBS, with only 20.2% cumulative release of eosin over 72 h at 37 °C. In contrast, GSH exposure led to significantly accelerated dye release: within 6 h, the release was already significantly increased ($p < 0.05$), and by 72 h, the cumulative release was 3.6-fold higher compared to PBS alone ($p < 0.001$; Fig. 1l).

We assessed the antagonistic activity of GRIP-derived NPs, both intact NP_{CMC} (as a prodrug form) and GSSEA (as the active product), on iNOS activity using iNOS assay kits. While NP_{CMC} did not alter iNOS activity even at concentrations up to 50 μM, GSSEA led to a significant decrease in enzyme activity at both 10 μM and 50 μM compared to the control group ($p < 0.05$ and $p < 0.01$, respectively; Fig. 1m).

These findings align with the mechanistic activation of GRIP upon its reaction with GSH (Fig. 1e and k). Following reaction with two molecules of GSH, one converts to GSSEA while the other disrupts the ionic interactions between GRIP and the anionic payload of the NPs, resulting in enhanced release. This system can modulate the TME for more selective and targeted treatment, particularly in tumors with elevated GSH levels compared to normal tissues, such as pancreatic tumors [23]. In the context of tumor therapy, this depletion of GSH may be advantageous, as reduced GSH levels have been shown to improve therapeutic outcomes in such tumors [24].

Given that iNOS is an intracellular enzyme and GSH level is almost 1000-fold higher in intracellular fluids than extracellular ones [21], it is important to determine whether the NPs can effectively enter cells. To assess cellular uptake, GRIP was formulated with a fluorescent dye (Cy5.5) to form a traceable NP ($NP_{Cy5.5}$). As shown in Fig. 1m, a 4h incubation with $NP_{Cy5.5}$ resulted in substantial cellular uptake of the NPs (red). The fluorescence distribution differed from that of LysoTracker (green), and co-localization analysis revealed a non-diagonal overlap with the LysoTracker signal (Fig. 1n). This suggests that $NP_{Cy5.5}$ was likely undergoing partial lysosomal uptake within the cells or was sufficiently stable to escape lysosomal degradation. Although identifying the exact mechanism by which the NPs escape from lysosomes requires further investigation and is beyond the scope of this study, it is noteworthy that the concentration of low-molecular-weight thiols, particularly GSH, is significantly lower in lysosomes than in the cytosol [25]. Consequently, the NPs may remain largely inactive within the lysosomal environment but undergo rapid activation once they reach the cytosol, where GSH levels are in the millimolar range.

The structural basis for GSSEA inhibition was investigated by docking GSSEA into the catalytic domain of human iNOS (PDB code 4NOS) [26] using SwissDock 2024 [11, 12]. As shown in Fig. 2a and b, GSSEA binds within the iNOS active site in a conformation that closely overlaps with crystal structures of iNOS-inhibitor complexes. Specifically, the docking analysis reveals GSSEA forming bidentate hydrogen bonds with the side chain of Glu 377 (Fig. 2c), a catalytically important residue known to be involved in substrate binding [26, 27]. Similar interactions are observed in the crystal structures of complexes between human iNOS with aminopyridine inhibitors (Fig. 2d-e) [28]. Additional hydrogen bonds are seen between the aminopyridine inhibitors and the backbone carbonyl of Trp 372 (Fig. 2d) or the side chain of Tyr 437 (Fig. 2e), both of which are conserved in the predicted iNOS-GSSEA structure (Fig. 2c).

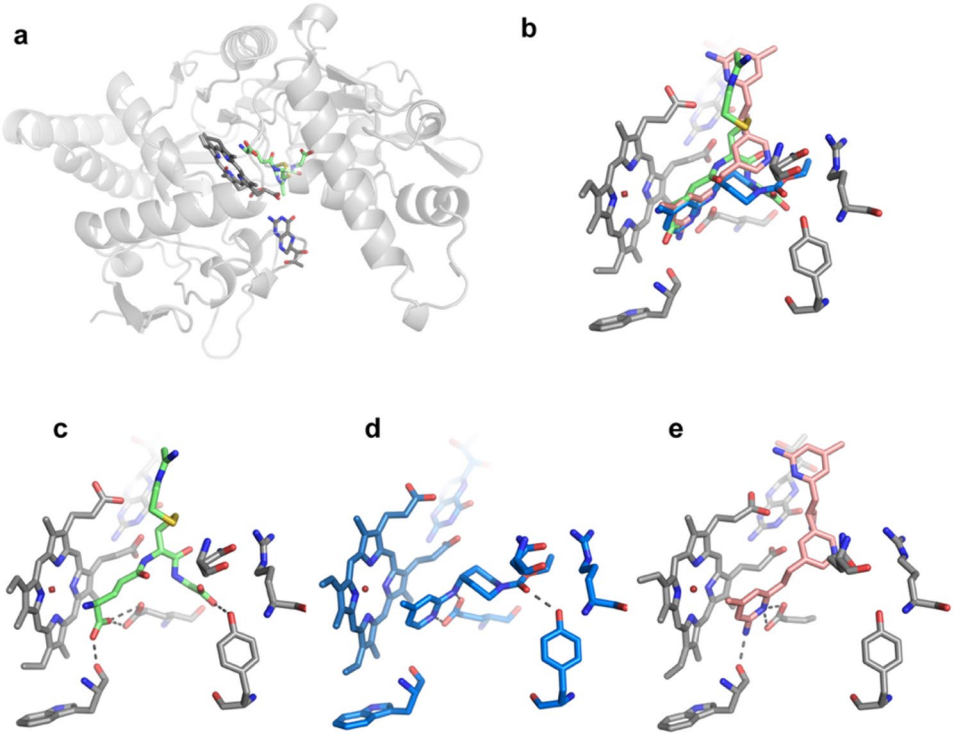

Fig. 2 Docking of GSSEA to human iNOS. (**a**) Catalytic domain of human iNOS (PDB code 4NOS) with the heme and tetrahydrobiopterin shown in stick representation. The docked GSSEA molecule (green) binds close to the heme. (**b**) Zoomed-in showing how the GSSEA binding site overlaps with previously published crystal structures of iNOS in complex with aminopyridine inhibitors (4CX7-salmon, 3EG7-blue). **c**-**e** Comparison of predicted interactions in the iNOS-GSSEA docking model (**c**) and iNOS-aminopyridine inhibitor crystal structures (**d**-**e**)

These findings suggest that cystamine-based disulfide linkers can function as glutathione-responsive moieties. Upon exposure to GSH, these linkers alter NP stability, facilitating enhanced release of the encapsulated anionic compound. Additionally, upon activation, the GRIP system converts intracellular GSH into an iNOS antagonist. This dual functionality holds significant promise for targeted tumor therapy.

As GRIP activation is mediated by disulfide bond cleavage, it may also occur in the presence of other intracellular thiols, such as cysteine. However, intracellular concentrations of GSH are typically an order of magnitude higher than those of cysteine, particularly in certain cancer cells, including pancreatic tumors, where GSH levels are significantly elevated relative to normal cells. In animal cells, GSH concentrations generally range from 0.5 to 10 mM, whereas cysteine concentrations are much lower, typically 150–250 μM [25]. Indeed, cysteine is among the least abundant amino acids within cells [29]. Consequently, GRIP activation by GSH is substantially more likely than activation by other thiols.

Furthermore, docking of the reaction product formed between GRIP and cysteine (CySSEA) revealed interaction profiles distinct from those of GSSEA. Specifically, CySSEA does not form the key hydrogen bonds observed for GSSEA with Trp372 or with the side chain of Tyr437 in iNOS (Figure S7).

Applying GRIP for the delivery of betamethasone

Glucocorticoids exhibit diverse biological effects on mammalian cells, including immunosuppressive and anti-inflammatory actions, as well as the induction of apoptosis, necrosis, and anti-angiogenic activity [30]. These multifaceted mechanisms contribute to the antitumor properties of glucocorticoids through both genomic and non-genomic pathways [31]. However, most synthetic glucocorticoids are hydrophobic and exhibit poor pharmacokinetic profiles for effective tumour therapy [32]. To demonstrate that GRIP can carry hydrophobic therapeutic agents bearing acidic functional groups, we developed a formulation of GRIP and Betamethasone succinate (BeS) via polyionic interactions, termed NP_{BeS}, with an average size of 176 nm (Fig. 3a-b). These particle showed neutral surface charge with a zeta potential of 0.6 ± 4.6 and PDI of 0.19 ± 0.1 (Fig. 3c). We then assessed the effects of GRIP, GSSEA, free BeS, and NP_{BeS} on the viability of monocytes (RAW264.7; Fig. 3d) after 24 h of treatment. GSSEA did not show any cytotoxic effects up to 100μM, while GRIP at 100μM resulted in a significant 26% decrease in cell viability ($p < 0.01$). This cytotoxic effect may result from the cationic nature of GRIP, which can disrupt cell membrane stability and lead to cellular toxicity [33]. Both BeS and NP_{BeS} showed significant toxicity starting from 50μM compared to the control ($p < 0.05$), with no significant difference observed between BeS and NP_{BeS}.

Inhibition of NO overproduction in cells

Treating RAW264.7 monocytes with LPS (500 ng/mL for 24 h) polarized them toward M1 macrophages, resulting in significant iNOS expression [34]. This polarization was associated with a marked increase in intracellular NO levels, as detected by the NO-specific fluorescent probe DAF-2Da (Fig. 3e-f) [35]. Exposing these LPS-pretreated cells to 10 μM BeS or NP_{BeS} for 3 h did not alter NO levels. In contrast, GSSEA treatment under the same conditions significantly reduced NO production. Despite the notable cellular uptake of NP_{BeS} within this timeframe (Fig. 1n), these findings suggest that NP_{BeS} functions as a prodrug, requiring a longer duration for activation within the cells. The observed decrease in NO levels with GSSEA may be attributed to its antagonistic activity on iNOS.

Under similar conditions, where cells were co-treated with LPS and GSSEA, BeS, or NP_{BeS} for 24 h, all the treatments resulted in a significant decrease in intracellular NO levels (Fig. 3g-h). Similar results were observed measuring the total nitrite (metabolite of NO and O_2) in the cell culture medium using Griess assay (Figure S8). This effect is likely due to a combination of direct antagonism of iNOS enzymatic activity and downregulation of iNOS expression, as confirmed by western blot (Fig. 3i, Figure S9). Corticosteroids such as BeS are recognized for their potent ability to inhibit iNOS expression at the transcriptional level. Upon ligand binding, BeS activates glucocorticoid receptors, which translocate to the nucleus and interfere with pro-inflammatory transcription factors such as NF-κB and AP-1, thereby suppressing iNOS gene expression [36]. Notably, GSSEA significantly reduced the iNOS expression level (Figure S9), which may be a consequence of its antagonistic effect on iNOS activity. This is consistent with previous reports showing that classical iNOS antagonists can downregulate iNOS expression in the cells [37, 38].

Inhibition of aberrant migration

NO exerts a multifaceted and context-dependent influence on cell migration and metastasis, functioning as a promoter and inhibitor of tumor progression depending on its concentration, exposure duration, and the cellular environment [39]. NO can facilitate cancer cell migration and invasiveness by modulating key signaling pathways, including PI3K/Akt, MAPK, and mTOR, and by inducing cytoskeletal reorganization, processes critical for metastasis [39, 40]. For instance, prolonged NO exposure in lung cancer cells has been shown to enhance migratory behavior through upregulation of caveolin-1 and activation of focal adhesion kinase (FAK) and Akt signaling

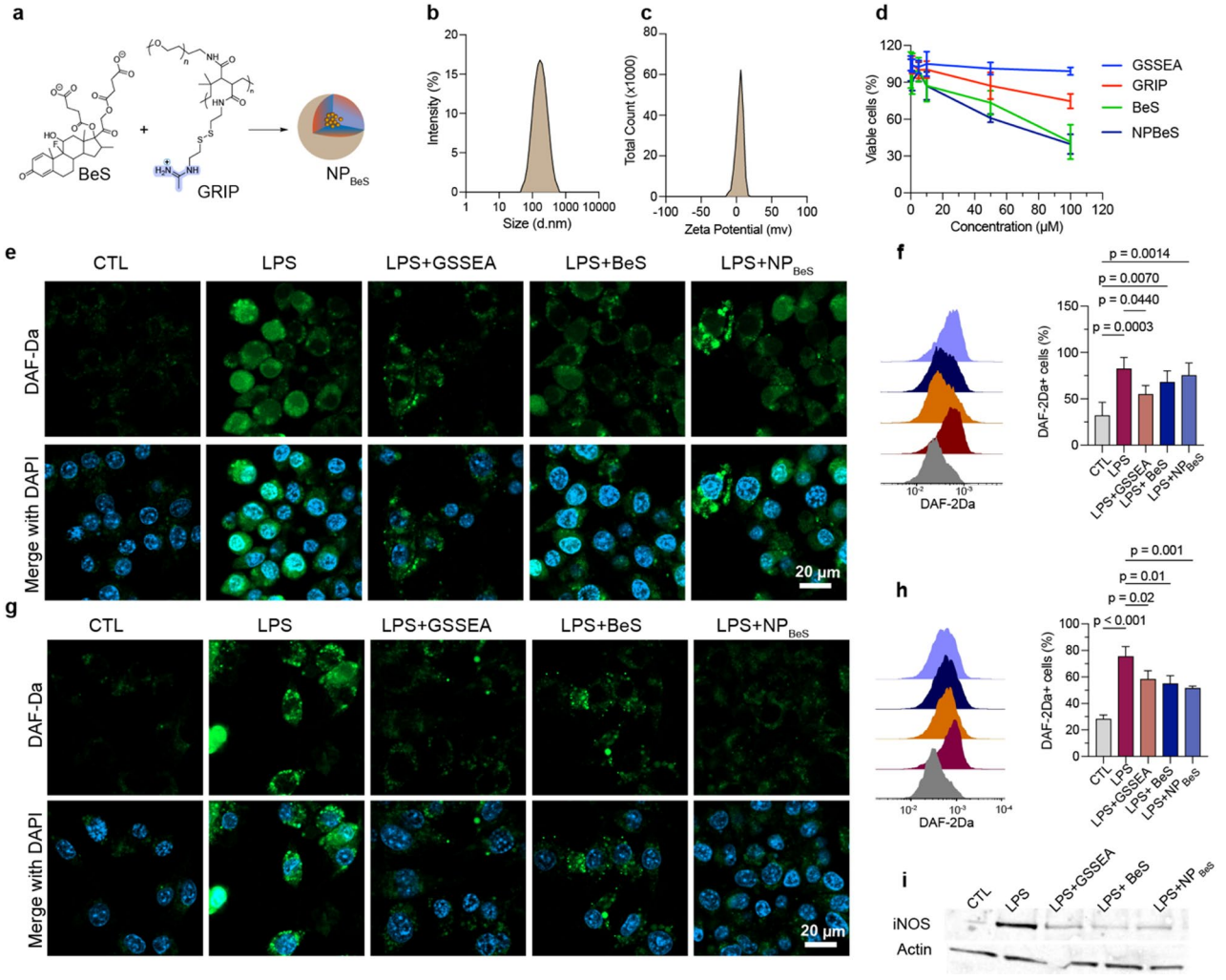

Fig. 3 GRIP-based NPs function as GSH-responsive iNOS antagonists. **(a)** Mechanism of NP_{BeS} (nanoparticles of betamethasone succinate) synthesis via interaction between GRIP and BeS. **(b)** NP_{BeS} in aqueous solution with an average size of 176 nm. **(c)** Zeta potential of NP_{BeS} shows nutral surface charge. **(d)** Effects of GRIP, GSSEA, BeS, or NP_{BeS} on the cell viability of RAW 267.4 macrophages after 24 h of incubation. **e-h.** Effects of 3 h (**e-f**) or 24 h (**g-h**) incubation with LPS alone or in combination with GSSEA, BeS, or NP_{BeS} on NO production in RAW 267.4 cells using DAF-2Da (green). Nuclei were stained with DAPI (blue). **i.** Representative Western blot of the treated cells for 24 h (statistical analysis shown in Figure S9). Results are expressed as mean ± SD ($n = 3$). Differences were considered significant if $p < 0.05$

pathways [41]. NO is a critical downstream mediator of VEGF-induced angiogenesis and migration, facilitating endothelial cell proliferation, survival, and motility through both cGMP-dependent and independent pathways, ultimately supporting neovascularization [42].

To assess the effects of our compounds on cell migration, we performed a standard scratch assay using 3T3-L1 fibroblast cells. VEGF (50 ng/ml) increased cell migration, as indicated by a significantly smaller gap compared to the control after 12 h of incubation ($p < 0.01$; Fig. 4a–b). Both GSSEA and BeS prevented the proliferative and migratory effects of VEGF, though not significantly. In contrast, NP_{BeS} treatment resulted in a significantly larger gap compared to the VEGF group alone ($p < 0.05$). This is in agreement with previous studies showing NOS knockout or pharmacological inhibition of eNOS or iNOS impairs VEGF-induced cell migration [43].

Epithelial–mesenchymal transition (EMT) is a cellular program wherein epithelial cells undergo phenotypic changes, losing apical–basal polarity and intercellular adhesion, while acquiring mesenchymal characteristics such as enhanced motility and invasiveness [44]. This process is regulated by microenvironmental signals and involves coordinated alterations in gene expression and post-translational mechanisms that repress epithelial markers and activate mesenchymal programs. One of the classical hallmarks of EMT is vimentin, which is highly overexpressed in EMT, as well as aggressive tumors [45, 46]. VEGF and vimentin interact synergistically to promote angiogenesis and migration. VEGF increases

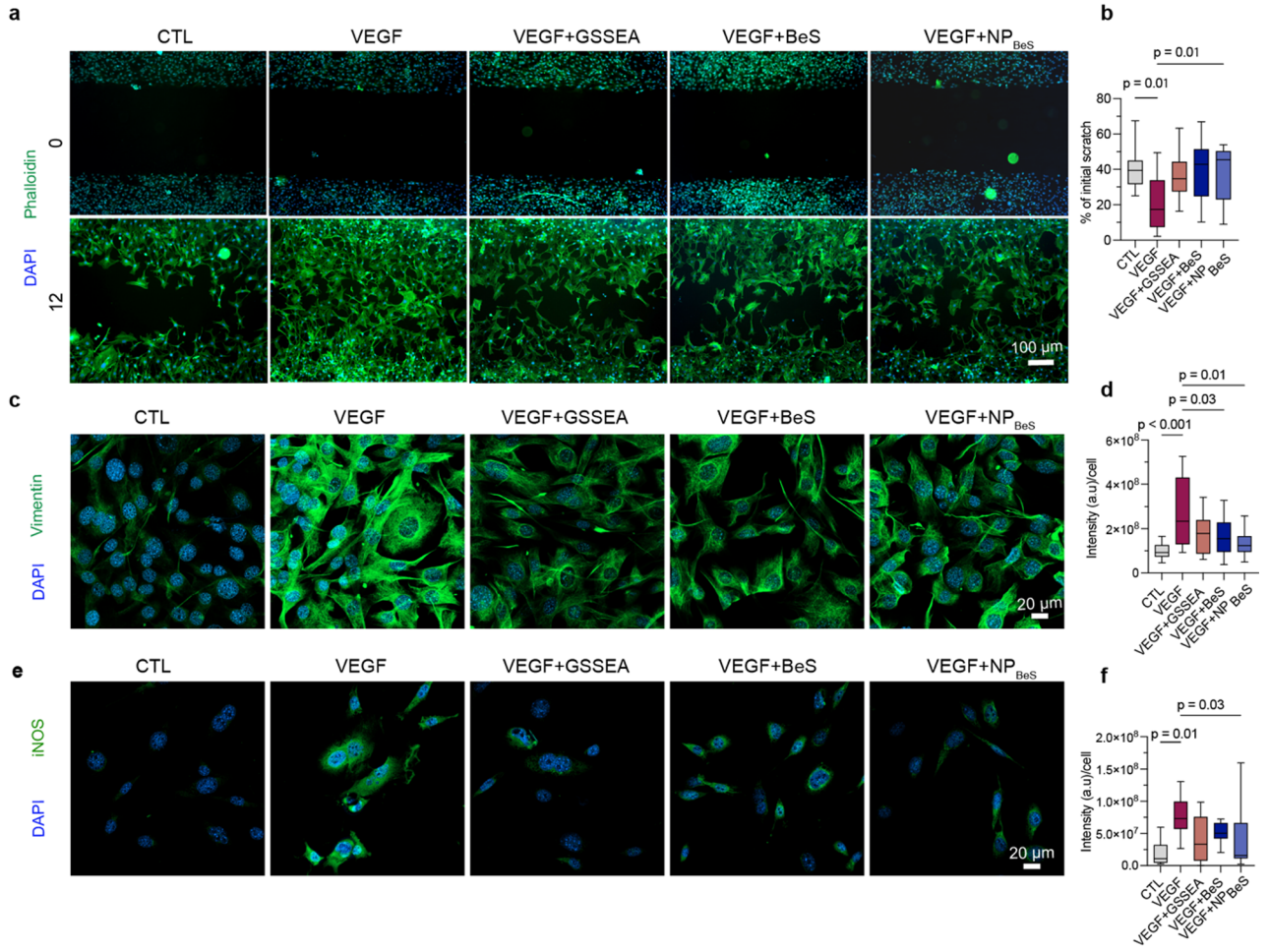

Fig. 4 Effects of the formulations on cell proliferation, migration, and iNOS expression. **a-b.** VEGF at 50 ng/mL significantly increases the cell proliferation and migration of 3T3-L1 cells. Treatment with GSSEA, BeS, or particularly by NP_{BeS} reduces VEGF-induced proliferation and migration. F-actin of the cells were stained with phalloidin (green) to present representative images of cells in scratch assay. Cells nuclei are stained in blue with DAPI **c-d.** VEGF increases vimentin expression (green) in 3T3-L1 cells, which is inhibited by GSSEA, BeS, and particularly by NP_{BeS}. **e.** VEGF induces iNOS expression (green) in the cells, which can be inhibited by all three treatments, with NP_{BeS} showing the strongest inhibitory effect. Data are presented as median with range ($n = 10$). Statistical analysis was performed using the Kruskal-Wallis test (non-parametric one-way ANOVA) followed by Dunn's multiple comparison test. Differences were considered significant if $p < 0.05$

vimentin secretion in endothelial cells, while vimentin binds to VEGFR2 and potentiates VEGF signaling [45, 46]. In 3T3-L1 cells, VEGF significantly upregulated vimentin expression ($p < 0.001$), which was decreased by GSSEA, BeS, and more prominently by NP_{BeS} ($p < 0.01$) (Fig. 4c-d). Immunofluorescent staining of iNOS under the same conditions confirmed that VEGF upregulates iNOS expression, which can be inhibited by all three treatments, with the most pronounced effect observed in the NP_{BeS} group (Fig. 4e-f). Although the role of NO in EMT is controversial and multifactorial [47], in some cancers, such as metaplastic breast cancer, tumors are enriched in EMT and cancer stem cell features and predominantly exhibit aberrations in both the PI3K and iNOS pathways. Notably, recent clinical studies indicated that NOS inhibition sensitizes these tumors to PI3K inhibitors and taxane-based therapies, significantly reducing the metastasis [48].

Inhibition of angiogenesis

The antiangiogenic properties of the developed NP_{BeS} formulations were assessed by evaluating the ability of HUVECs to form capillary-like structures on Matrigel. This method is widely used to study pro- or anti-angiogenic compounds, as it replicates key angiogenesis processes, including endothelial cell differentiation, migration, alignment, and formation of tubular networks [49]. After 24 h of incubation, VEGF stimulation significantly increased the number of segments (1.8 fold), meshes (2.5 fold), and junctions (1.7 fold) in the capillary-like structures compared to the control (Fig. 5a-d). Co-treatment of VEGF with GSSEA, BeS, or

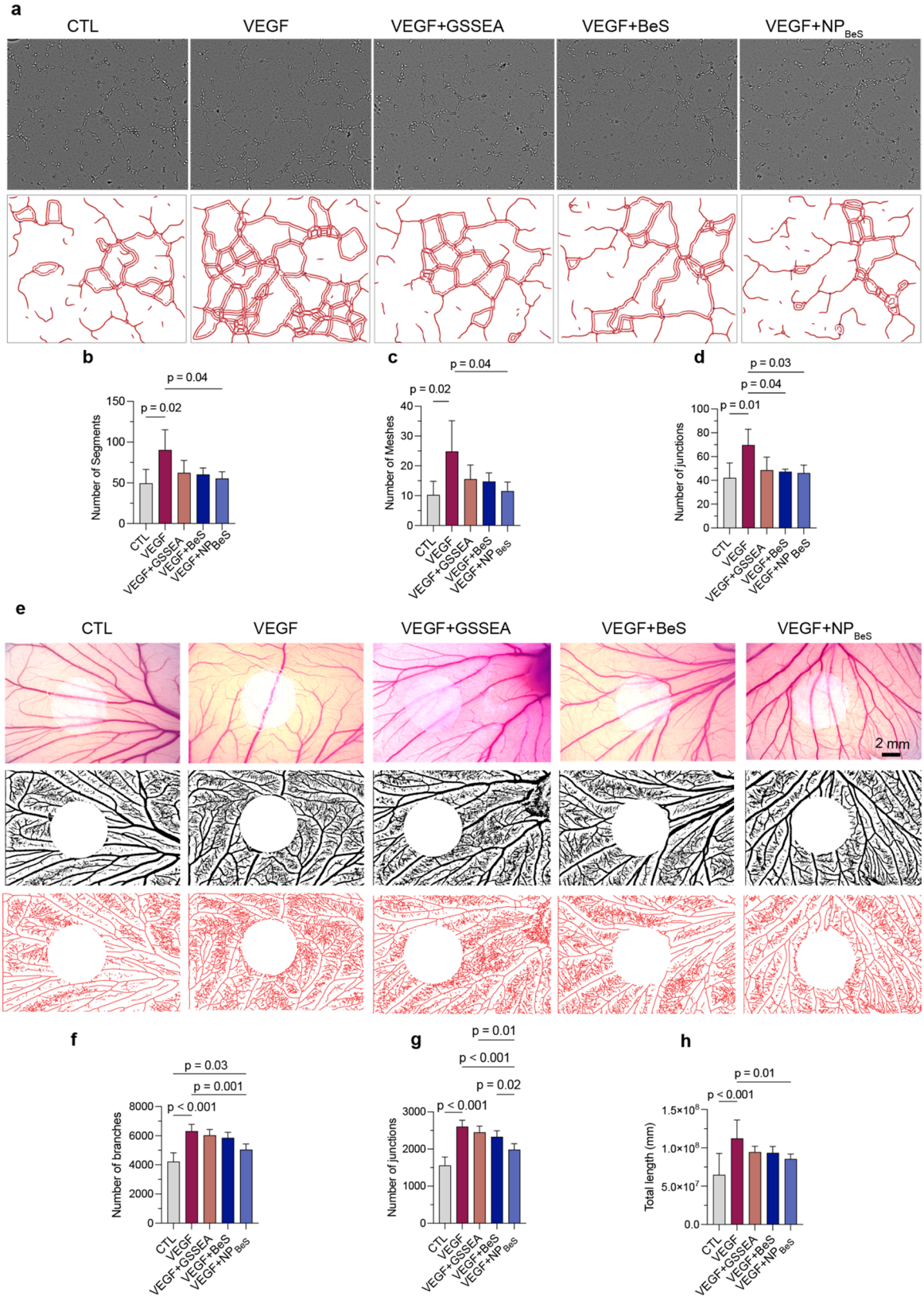

Fig. 5 (See legend on next page.)

(See figure on previous page.)

Fig. 5 Effects on angiogenesis in vitro and in the chick chorioallantoic membrane (CAM) assay. **a.** Phase contrast microscopy tube formation in HUVEC cultures following treatment with VEGF (50 ng/ml) alone or in combination with GSSEA, BeS, or NP_{BeS}. The bottom panel shows the detected tubes by the image analyzer. **b-d.** VEGF resulted in a significant increase in the number of segments, meshes, and junctions compared to the control (CTL). Treatment with NP_{BeS} resulted in significant inhibitory effects in VEGF-induced tube formation. **e.** Representative images from the CAM assay (top row), followed by processed images with background subtraction and brightness adjustment (middle row), and corresponding skeletonized vessel networks (bottom row). **f-h.** Quantification of number of branches, number of junctions, and total vessel length in the treated CAMs. Data are expressed as mean ± SD ($n = 6$) and analyzed using one-way ANOVA followed by Tukey's post hoc test. Differences were considered significant if $p < 0.05$

particularly NP_{BeS} resulted in a significant decrease in tube formation when compared with VEGF alone. These significant reductions highlight the efficacy of all three agents, especially NP_{BeS}, in counteracting VEGF-driven angiogenic processes.

Furthermore, the CAM assay (Fig. 5e), a well-established, cost-effective, and widely recognized model for studying blood vessel formation [50], was used to assess the anti-angiogenic effects of the test compounds. To this end, after 60 h of incubation, embryos were transferred to clean weighing boats and kept for an additional 24 h to remove damaged or dead embryos (approximately 29%) before treatment. None of the treatments caused any mortality in the tested embryos within 24 h (Figure S10). As expected, VEGF administration significantly increased the number of vessel branches, junctions, and total length of new blood vessels formed ($p < 0.001$; Fig. 5f-h). For example, VEGF induced a 1.6-fold increase in the number of junctions, which was significantly inhibited by co-treatment with NP_{BeS} ($p < 0.001$, Fig. 5g). In addition, VEGF + NP_{BeS} treatment showed significantly less number of junctions when compared with VEGF + BeS ($p < 0.05$) or VEGF + GSSEA ($p < 0.01$), suggesting NP_{BeS} may exert a more robust or possibly synergistic inhibitory effect on angiogenesis.

This anti-angiogenic effect is associated with a reduction in NO levels, a key regulator in cell proliferation, migration, and new blood vessel formation. Although eNOS plays a predominant role in VEGF-induced angiogenesis [51], iNOS inhibition still produces a measurable and additive reduction in angiogenesis. This highlights the therapeutic potential of iNOS antagonists in pathological neovascularization. Our data align with previous findings where iNOS antagonists are recognized as inhibitors of angiogenesis. For instance, experimental studies have demonstrated that selective inhibition of iNOS activity by compounds such as aminoguanidine, 1400 W, and L-NIO leads to a significant reduction in tumor angiogenesis, as evidenced by decreased microvessel density and VEGF expression in tumor models [52, 53].

Effects on vascular tone

One of the main challenges in developing anti-angiogenic therapies based on NO results from its critical role in maintaining vascular homeostasis [54]. The lack of NO in the cardiovascular system can result in severe vasoconstriction and elevated blood pressure [55], and prolonged therapies that lower NO levels may contribute to atherosclerosis [54]. Hence, it is critically important to assess the effects of novel iNOS-targeting agents on vascular function. In intact vessels, ACh binds to muscarinic receptors, primarily M_3, on endothelial cells, elevating intracellular calcium levels and activating eNOS-mediated NO synthesis. The generated NO diffuses to the underlying smooth muscle cells, triggering vascular smooth muscle relaxation through activation of multiple downstream pathways (Fig. 6a). Inhibiting eNOS disrupts this process and promotes vasoconstriction. To evaluate vascular tone, thoracic aorta segments were first contracted with 80 mM KCl. After washout, vessels were pre-contracted with PE (1 µmol/L), followed by ACh (0.1µM) to stimulate eNOS-derived NO. Subsequently, vessels were exposed to either PBS (CTL), L-NIO (a non-selective NOS inhibitor, positive control), GSSEA (active iNOS inhibitor), or GRIP (inactive form). L-NIO caused a 60% contraction at 10 µM ($p < 0.01$), which was further increased at 100 µM (Fig. 6c, f), consistent with previous reports demonstrating its potent vasoconstrictive effects in isolated vessel assays by effectively inhibiting NO synthesis and thereby impairing endothelium-dependent relaxation [55]. GRIP did not affect vascular tone at concentrations up to 100 µM (Fig. 6d and f). The active form of GRIP, GSSEA, induced around a 20% increase in average vascular tone compared to control; however, the difference was not statistically significant ($p > 0.05$, Fig. 6e and f). Importantly, after washout, none of the treatments affected the vessel responsiveness to PE, ACh, or KCl at the end of the experiment, indicating the safety of the tested compounds.

Conclusion and future directions

In this study, we, for the first time, developed GRIP and demonstrated its potential as an innovative anti-angiogenic therapy. GRIP can form polyionic nanoparticles with a range of anionic drugs or polymers and acts as a stimuli-responsive carrier. Its ability to inhibit iNOS while simultaneously delivering a payload offers a unique toolbox for treating complex conditions, particularly cancers in which iNOS plays a key role in disease pathophysiology.

NP_{BeS} (composed of GRIP and BeS) effectively inhibits aberrant angiogenesis in both in vitro and in ovo models by targeting iNOS and synergizing with BeS, while

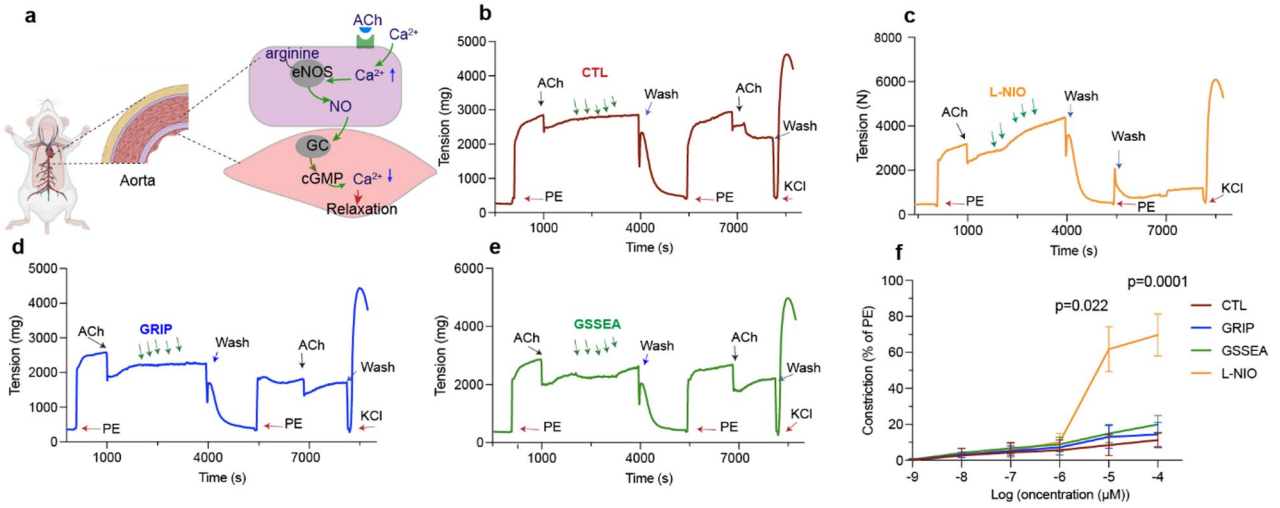

Fig. 6 Effects on aortic reactivity. **a.** Schematic representation of acetylcholine (ACh)-induced relaxation in rat aortic rings. ACh activates its receptors, which in turn activate eNOS to produce NO. Created by BioRender.com. **b-e.** Representative time course of the vessel responses to various pharmacological interventions. Vessel contractility was initially tested by sequential exposure to KCl and phenylephrine (PE). Vessels responsive to ACh (at least 65% of the contraction induced by PE) were considered endothelium-intact (Figure S11). The effects of treatments on vessel reactivity were normalized to the vasoconstriction induced by 1 μM PE. **f.** The effects of GRIP and its active form, GSSEA, on aortic reactivity were evaluated. Unlike GRIP and GSSEA, L-NIO impaired the vessel reactivity in response to PE. Data are expressed as mean ± SD ($n = 4$). Differences were considered significant if $p < 0.05$Created by BioRender.com

exhibiting minimal impact on vascular tone, addressing a key limitation of non-specific NOS inhibitors.

Given the elevated GSH levels in some tumors and the multifaceted role of NO in angiogenesis and EMT, GRIP-based NPs offer a promising strategy for controlled, tumor-specific vessel normalization. Furthermore, due to the cationic nature of GRIP, they can be used for the controlled delivery of a wide range of anticancer agents bearing anionic functional groups as well as genetic materials. These findings pave the way for further preclinical and clinical investigations aimed at enhancing the efficacy of anti-angiogenic cancer therapies.

Despite the innovative approach and the successful demonstration of proof of concept, this study has some limitations that will be addressed in future work. Further investigation regarding molecular dynamics simulations could provide valuable insights into the dynamic behavior, stability, and mechanistic interactions between the antagonist and iNOS. Because the utility of polymeric prodrugs depends heavily on their degradation kinetics, future studies will incorporate detailed characterization of GRIP cleavage and payload release kinetics, for example using HPLC-MS analysis, to better inform in vivo dosing strategies. It will also be essential to evaluate the therapeutic efficacy of NPBeS in tumor models characterized by elevated GSH levels, such as pancreatic ductal adenocarcinoma (PDAC). In these models, assessing the ability of GRIP-based NPs to accumulate in tumors via both the enhanced permeability and retention (EPR) effect and GSH-triggered activation will provide important information regarding their translational potential. Comprehensive profiling of immune responses, tumor blood flow and angiogenic marker expression within the TME will also help clarify the mechanistic impact of the system. In addition, although it is a well-established EMT marker [45, 46], assessing other markers such as E-cadherin, N-cadherin, and ZO in vitro and in vivo would further strengthen the evaluation of the NPs' effects on EMT. These aspects will be systematically examined in future studies using GRIP.

Abbreviations

AC	Attracting Cavities (SwissDock score)
ACh	Acetylcholine
AP-1	Activator protein-1
BCA	Bicinchoninic acid (protein assay)
BeS	Betamethasone succinate
BOC	Tert-butyloxycarbonyl (protecting group)
CAM	Chorioallantoic membrane (assay)
CMC	Carboxymethyl cellulose
CTL	Control
Cy5.5	Cyanine 5.5 (fluorescent dye)
DAF-2Da	4,5-diaminofluorescein-2 diacetate (NO probe)
DAPI	4′,6-diamidino-2-phenylindole (nuclear stain)
DLS	Dynamic light scattering
DMEM	Dulbecco's Modified Eagle Medium
DMSO	Dimethyl sulfoxide
DTT	Dithiothreitol
ECL	Enhanced chemiluminescence
EDC	1-ethyl-3-(3-dimethylaminopropyl)carbodiimide
eNOS	endothelial nitric oxide synthase
EMT	Epithelial–mesenchymal transition
Et_3N	Triethylamine
FAK	Focal adhesion kinase
FBS	Fetal bovine serum
FGF	Fibroblast growth factor
GRIP	Glutathione-responsive iNOS-inhibiting polymeric prodrug
GSSEA	Glutathione-derived disulfide ethyl acetimidamide
GSH	Glutathione

HEPES	4-(2-hydroxyethyl)-1-piperazineethanesulfonic acid
HRMS	High resolution mass spectroscopy
HRP	Horseradish peroxidase
HUVEC(s)	Human umbilical vein endothelial cell(s)
iNOS	inducible nitric oxide synthase
LPS	Lipopolysaccharide
MAPK	Mitogen-activated protein kinase
mTOR	mechanistic target of rapamycin
MTT	3-(4,5-dimethylthiazol-2-yl)-2,5-diphenyltetrazolium bromide
NADPH	Nicotinamide adenine dinucleotide phosphate (reduced form)
NF-κB	Nuclear factor kappa-light-chain-enhancer of activated B cells
NHS	N-hydroxysuccinimide
NMR	Nuclear magnetic resonance
NO	Nitric oxide
NP(s)	Nanoparticle(s)
NP_{BeS}	Nanoparticles made of GRIP and betamethasone succinate
NP_{Eosin}	Nanoparticles made of GRIP and eosin
PDB	Protein data bank
PEG	Polyethylene glycol
PE	Phenylephrine hydrochloride
PIMA	Poly(isobutylene-alt-maleic anhydride)
PI3K	Phosphoinositide 3-kinase
PVDF	Polyvinylidene difluoride (membrane)
RAW264.7	Murine macrophage cell line
SD	Standard deviation
SDS-PAGE	Sodium dodecyl sulfate–polyacrylamide gel electrophoresis
TFA	Trifluoroacetic acid
TEM	Transmission electron microscopy
TGF	Transforming growth factor
TME	Tumor microenvironment
VEGF	Vascular endothelial growth factor
VEGFR2	Vascular endothelial growth factor receptor 2

Supplementary Information

The online version contains supplementary material available at https://doi.org/10.1186/s12951-026-04022-z.

SI

Acknowledgements

This project receives funding from the European Union's Horizon 2020 research and innovation programme under the Marie Skłodowska-Curie Grant Agreement No 101034324, as well as a grant from the Fondation Jaumotte-Demoulin. Some of the equipment used in this study was financed, in whole or in part, by the Walloon Region through the Technology Platforms of Excellence: 'Alternative to animal experimentation' and 'Biogreen'. The authors gratefully acknowledge the Centre d'Instrumentation en Resonance Magnétique (CIREM) at Université libre de Bruxelles (ULB), Belgium, for access to infrastructure and technical support. The NMR spectrometer J400 used in this work was funded by the Fonds de la Recherche Scientifique (F.R.S.-FNRS–GEQ2011-2.5014.12) and the Fonds d'Encouragement à la Recherche (FER-ULB). The Center for Microscopy and Molecular Imaging (CMMI) is supported by grant 411132-957270 from the European Regional Development Fund and the Walloon Region (Wallonia-Biomed; project "CMMI-ULB"). The authors thank Solene Kamagate and Louise Conrard (CMMI) for their participation to this work.

Author contributions

HA (Conceptualization, Formal analysis, Funding acquisition, Investigation, Methodology, Project administration, Resources, Supervision, Validation, Visualization, Writing – original draft, Writing – review & editing); AF (Formal analysis, Investigation, Methodology, Visualization, Writing – review & editing); PJ (Investigation); NB (Investigation); FG (Investigation, Project administration); HT (Writing – review & editing); STH (Investigation, Software, Visualization, Writing – original draft, Writing – review & editing); AS (Conceptualization, Funding acquisition, Methodology, Project administration, Resources, Supervision, Writing – review & editing); LD (Investigation, Methodology, Writing – review & editing); CD (Conceptualization, Funding acquisition, Methodology, Project administration, Resources, Supervision, Writing – review & editing).

Funding

This project receives funding from the European Union's Horizon 2020 research and innovation programme under the Marie Skłodowska-Curie Grant Agreement No 101034324, as well as a grant from the Fondation Jaumotte-Demoulin. Some of the equipment used in this study was financed, in whole or in part, by the Walloon Region through the Technology Platforms of Excellence: 'Alternative to animal experimentation' and 'Biogreen'. The NMR spectrometer J400 from Centre d'Instrumentation en Resonance Magnétique (CIREM) at Université libre de Bruxelles (ULB), Belgium, was funded by the Fonds de la Recherche Scientifique (F.R.S.-FNRS–GEQ2011-2.5014.12) and the Fonds d'Encouragement à la Recherche (FER-ULB). CMMI imaging center is supported by grant 411132–957270 from the European Regional Development Fund and the Walloon Region (Wallonia-Biomed; project "CMMI-ULB").

Data availability

The data supporting the findings of this study are available from the corresponding author upon reasonable request.

Declarations

Competing interests

The authors declare no competing interests.

Author details

[1]Laboratory of Pathophysiological and Nutritional Biochemistry (LPNB), Faculty of Medicine, Université Libre de Bruxelles, 808 Route de Lennik, Blg G/E CP 611, Brussels 1070, Belgium
[2]3BIO-BioMatter, École Polytechnique de Bruxelles, Université Libre de Bruxelles, Avenue F.D. Roosevelt, 50 - CP 165/61, Brussels 1050, Belgium
[3]Experimental Laboratory of Intensive Care, Université Libre de Bruxelles, 808 Route de Lennik, Blg G/E CP604, Brussels 1070, Belgium
[4]Laboratory of Physiology & Pharmacology, Université Libre de Bruxelles, 808 Route de Lennik, Blg G/E CP604, Brussels 1070, Belgium
[5]Nuffield Department of Women's and Reproductive Health, Medical Sciences Division, John Radcliffe Hospital, University of Oxford, Oxford OX3 9DU, UK
[6]Division of Biochemistry and Structural Biology, Lund University, Box 124, Lund 221 00, Sweden

Received: 27 September 2025 / Accepted: 2 January 2026
Published online: 30 January 2026

References

1. Liu Z-L, Chen H-H, Zheng L-L, Sun L-P, Shi L. Angiogenic signaling pathways and anti-angiogenic therapy for cancer. Signal Transduct Target Therapy. 2023;8:198.
2. Cao Y, Arbiser J, D'Amato RJ, D'Amore PA, Ingber DE, Kerbel R, Klagsbrun M, Lim S, Moses MA, Zetter B. Forty-year journey of angiogenesis translational research. Sci Transl Med. 2011;3:rv114113–114113.
3. Bergers G, Hanahan D. Modes of resistance to anti-angiogenic therapy. Nat Rev Cancer. 2008;8:592–603.
4. Jászai J, Schmidt MH. Trends and challenges in tumor anti-angiogenic therapies. Cells. 2019;8:1102.
5. Ziche M, Morbidelli L. Nitric oxide and angiogenesis. J Neurooncol. 2000;50:139–48.
6. Alimoradi H, Greish K, Gamble AB, Giles GI. Controlled delivery of nitric oxide for cancer therapy. Pharm Nanatechnol. 2019;7:279–303.
7. Anavi S, Tirosh O. iNOS as a metabolic enzyme under stress conditions. Free Radic Biol Med. 2020;146:16–35.
8. Kroll J, Waltenberger J. VEGF-A induces expression of eNOS and iNOS in endothelial cells via VEGF receptor-2 (KDR). Biochem Biophys Res Commun. 1998;252:743–6.
9. Namba T, Koike H, Murakami K, Aoki M, Makino H, Hashiya N, Ogihara T, Kaneda Y, Kohno M, Morishita R. Angiogenesis induced by endothelial nitric oxide synthase gene through vascular endothelial growth factor expression in a rat hindlimb ischemia model. Circulation. 2003;108:2250–7.

10. Kudo S, Nagasaki Y. A novel nitric oxide-based anticancer therapeutics by macrophage-targeted Poly (l-arginine)-based nanoparticles. J Controlled Release. 2015;217:256–62.
11. Bugnon M, Röhrig UF, Goullieux M, Perez MA, Daina A, Michielin O, Zoete V. SwissDock 2024: major enhancements for small-molecule Docking with attracting cavities and AutoDock Vina. Nucleic Acids Res. 2024;52:W324–32.
12. Röhrig UF, Goullieux M, Bugnon M, Zoete V. Attracting cavities 2.0: improving the flexibility and robustness for small-molecule Docking. J Chem Inf Model. 2023;63:3925–40.
13. Hanthazi A, Jespers P, Vegh G, Degroot G-N, Springael J-Y, Lybaert P, Dewachter L, Mc Entee K. Chemerin influences endothelin-and serotonin-induced pulmonary artery vasoconstriction in rats. Life Sci. 2019;231:116580.
14. Insua I, Wilkinson A, Fernandez-Trillo F. Polyion complex (PIC) particles: Preparation and biomedical applications. Eur Polymer J. 2016;81:198–215.
15. Ma X, Zhao T, Ren X, Lin H, He P. Recent progress in polyion complex nanoparticles with enhanced stability for drug delivery. Polymers. 2024;16:1871.
16. Meka VS, Sing MK, Pichika MR, Nali SR, Kolapalli VR, Kesharwani P. A comprehensive review on polyelectrolyte complexes. Drug Discovery Today. 2017;22:1697–706.
17. Merdan T, Kunath K, Petersen H, Bakowsky U, Voigt KH, Kopecek J, Kissel T. PEGylation of Poly (ethylene imine) affects stability of complexes with plasmid DNA under in vivo conditions in a dose-dependent manner after intravenous injection into mice. Bioconjug Chem. 2005;16:785–92.
18. Shi L, Zhang J, Zhao M, Tang S, Cheng X, Zhang W, Li W, Liu X, Peng H, Wang Q. Effects of polyethylene glycol on the surface of nanoparticles for targeted drug delivery. Nanoscale. 2021;13:10748–64.
19. Gamcsik MP, Kasibhatla MS, Teeter SD, Colvin OM. Glutathione levels in human tumors. Biomarkers. 2012;17:671–91.
20. Perry RR, Mazetta J, Levin M, Barranco SC. Glutathione levels and variability in breast tumors and normal tissue. Cancer. 1993;72:783–7.
21. Lee MH, Yang Z, Lim CW, Lee YH, Dongbang S, Kang C, Kim JS. Disulfide-cleavage-triggered chemosensors and their biological applications. Chem Rev. 2013;113:5071–109.
22. Ling X, Tu J, Wang J, Shajii A, Kong N, Feng C, Zhang Y, Yu M, Xie T, Bharwani Z. Glutathione-responsive prodrug nanoparticles for effective drug delivery and cancer therapy. ACS Nano. 2018;13:357–70.
23. Wu X, Yu R, Yang M, Hu Y, Tang M, Zhang S, Abudourousuli A, Li X, Li Z, Liao X. Integrated analysis of glutathione metabolic pathway in pancreatic cancer. Front Cell Dev Biology. 2022;10:896136.
24. Schnelldorfer T, Gansauge S, Gansauge F, Schlosser S, Beger HG, Nussler AK. Glutathione depletion causes cell growth Inhibition and enhanced apoptosis in pancreatic cancer cells. Cancer: Interdisciplinary Int J Am Cancer Soc. 2000;89:1440–7.
25. Wu G, Lupton JR, Turner ND, Fang Y-Z, Yang S. Glutathione metabolism and its implications for health. J Nutr. 2004;134:489–92.
26. Fischmann TO, Hruza A, Niu XD, Fossetta JD, Lunn CA, Dolphin E, Prongay AJ, Reichert P, Lundell DJ, Narula SK. Structural characterization of nitric oxide synthase isoforms reveals striking active-site conservation. Nat Struct Biol. 1999;6:233–42.
27. Gachhui R, Ghosh DK, Wu C, Parkinson J, Crane BR, Stuehr DJ. Mutagenesis of acidic residues in the Oxygenase domain of inducible nitric-oxide synthase identifies a glutamate involved in arginine binding. Biochemistry. 1997;36:5097–103.
28. Li H, Jamal J, Delker S, Plaza C, Ji H, Jing Q, Huang H, Kang S, Silverman RB, Poulos TL. The mobility of a conserved tyrosine residue controls isoform-dependent enzyme–inhibitor interactions in nitric oxide synthases. Biochemistry. 2014;53:5272–9.
29. Daher B, Vučetić M, Pouysségur J. Cysteine depletion, a key action to challenge cancer cells to ferroptotic cell death. Front Oncol. 2020;10:723.
30. Yano A, Fujii Y, Iwai A, Kageyama Y, Kihara K. Glucocorticoids suppress tumor angiogenesis and in vivo growth of prostate cancer cells. Clin Cancer Res. 2006;12:3003–9.
31. Garrido O, Letelier R, Rosas C, Fuenzalida M, Ferreira A, Lemus D. Betamethasone inhibits tumor development, microvessel density and prolongs survival in mice with a multiresistant adenocarcinoma TA3. Biol Res. 2010;43:317–22.
32. Luo L, Yang J, Oh Y, Hartsock MJ, Xia S, Kim Y-C, Ding Z, Meng T, Eberhart CG, Ensign LM. Controlled release of corticosteroid with biodegradable nanoparticles for treating experimental autoimmune uveitis. J Controlled Release. 2019;296:68–80.
33. Weiss AM, Lopez MA, Rawe BW, Manna S, Chen Q, Mulder EJ, Rowan SJ, Esser-Kahn AP. Understanding how cationic polymers' properties inform toxic or Immunogenic responses via parametric analysis. Macromolecules. 2023;56:7286–99.
34. Guha M, Mackman N. LPS induction of gene expression in human monocytes. Cell Signal. 2001;13:85–94.
35. Arita NO, Cohen MF, Tokuda G, Yamasaki H. Fluorometric detection of nitric oxide with diaminofluoresceins (DAFs): applications and limitations for plant NO research. Fluorometric detection of nitric oxide with diaminofluoresceins (DAFs): applications and limitations for plant NO research. Fluorometric detection of nitric oxide with diaminofluoresceins (DAFs): applications and limitations for plant NO research. Nitric Oxide Plant Growth Dev Stress Physiol. 2006:269–280. https://doi.org/10.1007/7089_2006_090
36. Pang Y, Fan L-W, Zheng B, Campbell LR, Cai Z, Rhodes PG. Dexamethasone and betamethasone protect against lipopolysaccharide-induced brain damage in neonatal rats. Pediatr Res. 2012;71:552–8.
37. Chanthaphavong RS, Loughran PA, Lee TY, Scott MJ, Billiar TR. A role for cGMP in inducible nitric-oxide synthase (iNOS)-induced tumor necrosis factor (TNF) α-converting enzyme (TACE/ADAM17) activation, translocation, and TNF receptor 1 (TNFR1) shedding in hepatocytes. J Biol Chem. 2012;287:35887–98.
38. Lee M, Choy JC. Positive feedback regulation of human inducible nitric-oxide synthase expression by Ras protein S-nitrosylation. J Biol Chem. 2013;288:15677–86.
39. Reddy TP, Glynn SA, Billiar TR, Wink DA, Chang JC. Targeting nitric oxide: say NO to metastasis. Clin Cancer Res. 2023;29:1855–68.
40. Lopez-Rivera E, Jayaraman P, Parikh F, Davies MA, Ekmekcioglu S, Izadmehr S, Milton DR, Chipuk JE, Grimm EA, Estrada Y. Inducible nitric oxide synthase drives mTOR pathway activation and proliferation of human melanoma by reversible nitrosylation of TSC2. Cancer Res. 2014;74:1067–78.
41. Saisongkorh V, Maiuthed A, Chanvorachote P. Nitric oxide increases the migratory activity of non-small cell lung cancer cells via AKT-mediated integrin αv and β1 upregulation. Cell Oncol. 2016;39:449–62.
42. Kimura H, Esumi H. Reciprocal regulation between nitric oxide and vascular endothelial growth factor in angiogenesis. Acta Biochim Pol. 2003;50:49–59.
43. Palumbo P, Lombardi F, Augello FR, Giusti I, Luzzi S, Dolo V, Cifone MG, Cinque B. NOS2 inhibitor 1400 W induces autophagic flux and influences extracellular vesicle profile in human glioblastoma U87MG cell line. Int J Mol Sci. 2019;20:3010.
44. Yang J, Antin P, Berx G, Blanpain C, Brabletz T, Bronner M, Campbell K, Cano A, Casanova J, Christofori G. Guidelines and definitions for research on epithelial–mesenchymal transition. Nat Rev Mol Cell Biol. 2020;21:341–52.
45. van Beijnum JR, Huijbers EJ, van Loon K, Blanas A, Akbari P, Roos A, Wong TJ, Denisov SS, Hackeng TM, Jimenez CR. Extracellular vimentin mimics VEGF and is a target for anti-angiogenic immunotherapy. Nat Commun. 2022;13:2842.
46. Kong D, Zhou H, Neelakantan D, Hughes CJ, Hsu JY, Srinivasan RR, Lewis MT, Ford HL. VEGF-C mediates tumor growth and metastasis through promoting EMT-epithelial breast cancer cell crosstalk. Oncogene. 2021;40:964–79.
47. Bonavida B, Baritaki S. Dual role of NO donors in the reversal of tumor cell resistance and EMT: downregulation of the NF-κB/Snail/YY1/RKIP circuitry. Nitric Oxide. 2011;24:1–7.
48. Reddy T, Puri A, Guzman-Rojas L, Thomas C, Qian W, Zhou J, Zhao H, Mahboubi B, Oo A, Cho Y-J. NOS Inhibition sensitizes metaplastic breast cancer to PI3K Inhibition and taxane therapy via c-JUN repression. Nat Commun. 2024;15:10737.
49. Ponce ML. Tube formation: an in vitro matrigel angiogenesis assay. In Angiogenesis protocols. Springer; 2009: 183–188.
50. Ribatti D, Annese T, Tamma R. The use of the chick embryo CAM assay in the study of angiogenic activiy of biomaterials. Microvasc Res. 2020;131:104026.
51. Smith TL, Oubaha M, Cagnone G, Boscher C, Kim JS, El Bakkouri Y, Zhang Y, Chidiac R, Corriveau J, Delisle C. eNOS controls angiogenic sprouting and retinal neovascularization through the regulation of endothelial cell Polarity. Cell Mol Life Sci. 2022;79:37.
52. Wang G-Y, Ji B, Wang X, Gu J-H. Anti-cancer effect of iNOS inhibitor and its correlation with angiogenesis in gastric cancer. World J Gastroenterology: WJG. 2005;11:3830.
53. Gao Y, Zhou S, Xu Y, Sheng S, Qian SY, Huo X. Nitric oxide synthase inhibitors 1400 W and L-NIO inhibit angiogenesis pathway of colorectal cancer. Nitric Oxide. 2019;83:33–9.
54. Infante T, Costa D, Napoli C. Novel insights regarding nitric oxide and cardiovascular diseases. Angiology. 2021;72:411–25.
55. Lankhorst S, Kappers MH, van Esch JH, Danser AJ, van den Meiracker AH. Hypertension during vascular endothelial growth factor inhibition: focus

on nitric oxide, endothelin-1, and oxidative stress. Antioxid Redox Signal. 2014;20:135–45.

Publisher's note

Springer Nature remains neutral with regard to jurisdictional claims in published maps and institutional affiliations.